ACS APPLIED NANO MATERIALS

Article

Cite This: ACS Appl. Nano Mater. 2019, 2, 214−227

www.acsanm.org

Competitive Effects of Structural Heterogeneity and Surface Chemical States on Catalytic Efficiency of FeSiBPCu Amorphous and Nanocrystalline Alloys

Qianqian Wang,[†] Lu Yun,[†] Mingxiu Chen,[†] Dandan Xu,[†] Zhiqiang Cui,[†] Qiaoshi Zeng,[†] Pinghua Lin,[†] Chenglin Chu,[†] and Baolong Shen*[,†,‡]

[†]School of Materials Science and Engineering, Jiangsu Key Laboratory for Advanced Metallic Materials, Southeast University, Nanjing 211189, China

[‡]Institute of Massive Amorphous Metal Science, China University of Mining and Technology, Xuzhou 221116, China

Supporting Information

ABSTRACT: The competitive effects of structural heterogeneity and surface chemical states on the catalytic efficiency of FeSiBPCu amorphous, single nanocrystalline, and multiple crystalline ribbons toward methylene blue (MB) degradation via Fenton-like reactions are studied. The FeSiBPCu amorphous and single nanocrystalline ribbons show higher catalytic efficiency than their multiple crystalline counterpart and FeSiB amorphous alloy. There are more Fe^0 and galvanic cell structures on the surfaces of FeSiBPCu single nanocrystalline ribbons than those of FeSiBPCu amorphous ribbons. However, the amorphous and single nanocrystalline ribbons show similar catalytic performance due to the passive iron phosphate and silica layer formed on the surfaces of FeSiBPCu single nanocrystalline ribbons during annealing. Formation of $Fe_3P_{0.37}B_{0.63}$ and enrichment of iron phosphates and silica on the surface reduces the catalytic efficiency of FeSiBPCu multiple crystalline ribbons. The dye degrading process finishes within 30 min using FeSiBPCu amorphous ribbons even after 20 recycles. This work clarifies the competitive effects of structural heterogeneity and change of surface chemical states induced by annealing on the catalytic efficiency of FeSiBPCu amorphous ribbons.

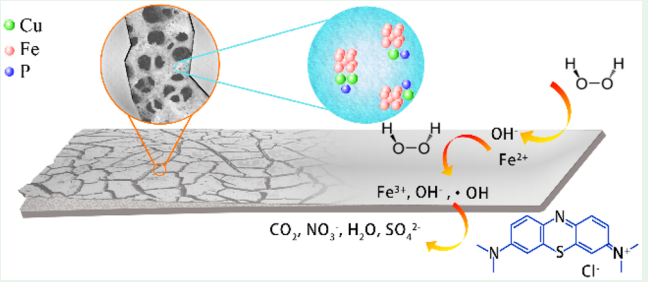

KEYWORDS: *structural heterogeneity, surface chemical states, catalytic efficiency, FeSiBPCu amorphous alloy, annealing*

1. INTRODUCTION

Zero-valent metal (ZVM), especially zero-valent iron (ZVI), has been proven to be an effective material for decomposition of groundwater pollutants including synthetic dyes and other organic contaminants.[1−4] An obvious improvement of the degradation ability has been noticed by introducing another metal with less chemical reactivity into ZVI to form bimetallic nanoparticles including Ni/Fe, Pd/Fe, Pt/Fe, and others, as the galvanic cells formed between iron and other metals accelerate the electron donation rate of iron.[5,6] However, the serious surface oxidation and high manufacturing cost of nanoparticles limits their widespread applications in wastewater treatment. Recently, Fe-,[7−18] Co-,[19,20] Mg-,[21−26] and Al-based[27,28] amorphous ribbons/powders have been proven to possess satisfying degradation ability toward organic contaminants in industrial wastewater because of their low reaction activation energy and a large amount of unsaturated sites coming from their metastable nature. The promoted degradation efficiency by the formed galvanic cells because of structural heterogeneity was also reported in amorphous alloys. Qin et al. reported that $Co_{78}Si_8B_{14}$ amorphous powders exhibited 3000 times higher degradation ability of azo dye than ZVI powders because of the formation of local galvanic couples between Si/B and Co.[19] Xie et al. found that the large atomic size of yttrium in $Fe_{76}Si_{12}B_9Y_3$ amorphous alloy induced a heterogeneous structure consisting of Fe-rich and Fe-poor regions to form galvanic cells, which tremendously improved the degradation efficiency of the alloy.[12] Recently, our group revealed that the excellent Fenton catalytic ability of $Fe_{80}P_{13}C_7$ amorphous ribbons for decolorization of methylene blue (MB) resulted from the fast electron transportation due to the galvanic cells formed between the weak Fe−P bonds and the strong Fe−C bonds.[29] Liang et al. found that the galvanic cells formed between multiphase intermetallics in fully crystallized $Fe_{78}Si_9B_{13}$ and $Fe_{73.5}Si_{13.5}B_9Cu_1Nb_3$ ribbons led to rejuvenation of their catalytic performance.[30]

On the other hand, $Fe_{83.3-84.3}Si_4B_8P_{3-4}Cu_{0.7}$ amorphous alloys have attracted a lot of research attention, as their nanocrystalline counterparts possess a high B_s of 1.88−1.9 T and a low H_c of 7−10 Am^{-1} and are considered as promising

Received: October 21, 2018
Accepted: December 21, 2018
Published: December 21, 2018

DOI: 10.1021/acsanm.8b01669
ACS Appl. Nano Mater. 2019, 2, 214−227

Fe-based soft magnetic materials.[31−33] The low solubility of Cu−P atomic pairs in iron, which comes from the coeffect of the positive mixing enthalpy of the Fe−Cu pair (+13 kJ/mol) and the negative mixing enthalpy of the Cu−P pair (−9 kJ/mol), induces chemical heterogeneity in the amorphous matrix and provides nucleation precursors for α-Fe, which is beneficial to the refinement of nanocrystalline grains during annealing.[34,35] As discussed above, the chemical inhomogeneity induced by Cu−P pairs can promote the formation of galvanic cell structures in the alloy; thus, the degradation performance of FeSiBPCu amorphous alloys should be promising.

Furthermore, there is disagreement about the effect of structural heterogeneity induced through annealing in Fe-based amorphous alloys on dye degradation efficiency. Some articles reported that the degradation efficiencies of alloys with multiple crystalline phases in amorphous matrix are significantly higher than those of pure amorphous alloys, while those of nanocrystallized alloys with a single crystalline phase dispersed in the amorphous matrix are lower than those of their amorphous counterparts. Wang et al. found that the numerous microbatteries formed between α-Fe(Si) and Fe_2B nanocrystalline phases in $Fe_{82.65}Si_4B_{12}Cu_{1.35}$ nanocrystalline alloy improved its efficiency by about 20% in decolorizing azo dye solution compared with the amorphous alloy or single nanocrystalline alloy.[27] Chen et al. found that the galvanic cells between α-Fe nanocrystals and the intermetallic compound formed during annealing contributed to the extremely high degradation efficiency toward Orange II in $(Fe_{73.5}Si_{13.5}B_9Nb_3Cu_1)_{91.5}Ni_{8.5}$ nanocrystalline alloys.[13] However, other works argued that the degradation efficiency was decreased by annealing because of the structural stabilization of the alloys, no matter if single or multiple crystalline phases were formed. Jia et al. found that the disordered atomic structure of amorphous $Fe_{78}Si_9B_{13}$ ribbons gave them higher catalytic efficiency than their annealed counterparts with either single or multiple crystalline phases.[36] The degradation ability of $Fe_{76}Si_{12}B_9Y_3$ powders decreased continuously with the increasing annealing temperature up to 1123 K (when all the crystallization processes finish) because of structural relaxation.[12] In addition, the chemical states of the alloy elements on the surfaces of the alloys during annealing changes tremendously,[37] and this should affect the degradation performances of the alloys, as the reactions are surface-mediated. However, few thorough investigations of the relationship between the surface chemical states of the alloys and their degradation properties have been reported. Thus, it is crucial to investigate the catalytic ability of FeSiBPCu soft magnetic alloys in both amorphous and crystallized states to clarify the effects of structural heterogeneity and surface chemical states.

In this work, in order to study the competitive effects of structural heterogeneity and surface chemical states on the catalytic efficiency of FeSiBPCu alloys, Fenton-like reactions for MB degradation with varied reaction parameters using amorphous, single nanocrystalline, and multiple crystalline FeSiBPCu ribbons were performed and compared with the widely investigated FeSiB amorphous ribbons. MB is a widely used synthetic dye in the textile and pharmaceutical industries, and the Fenton-like reaction has been proven to be an effective method for wastewater treatment.[38−40] The phases, nanostructures, and surface chemical states of FeSiBPCu amorphous/nanocrystalline ribbons were modulated by isothermal annealing at different temperatures and discussed together with their catalytic performance. The outstanding reusability of FeSiBPCu amorphous alloys was also evaluated and discussed. This work clarifies the competitive effects of structural heterogeneity and surface chemical states on the catalytic ability of FeSiBPCu alloys.

2. MATERIALS AND METHODS

2.1. Materials and Reagents. Alloy ingots with a nominal composition of $Fe_{81}Si_2B_{10}P_6Cu_1$ (at%) were prepared by induction melting of high-purity Fe (99.99% wt %), Si (99.99% wt %), B (99.999% wt %), Cu (99.99% wt %), and prealloyed Fe−P ingots (75 at% Fe and 25 at% P) in a high-purity argon atmosphere. Alloy ingots with a nominal composition of $Fe_{78}Si_9B_{13}$ (at%) were prepared by arc melting of high-purity Fe (99.99 wt %%), Si (99.99 wt %), and B (99.999 wt %) in a high-purity argon atmosphere. Ribbons with a thickness of ∼25 μm and a width of ∼2 mm were prepared using a single roller melt-spinning system, which was vacuumed to 5×10^{-3} Pa first and then filled with purified argon (99.999%). As-quenched ribbons were annealed at different temperatures to develop single nanocrystalline and multiple crystalline samples. The annealing was carried out by keeping the ribbons in a preheated tubular furnace at annealing temperature for 8 min in argon atmosphere followed by water quenching. The ribbons were cut into 1 cm long pieces for degradation experiments. Commercial available synthetic dye (methylene blue, AR grade) was purchased from Xiya Reagent. Sodium hydroxide (NaOH, AR grade) was purchased from Greagent. Sulfuric acid (H_2SO_4, AR grade) was purchased from Chron Chemicals. Hydrogen peroxide (H_2O_2, AR grade) was purchased from Sinopharm Chemical Reagent Co., Ltd. Tertiary butanol (TBA, CP grade) was purchased from Shanghai Lingfeng.

2.2. Characterization. Amorphous/crystalline phases and thermal stability of the ribbons were measured using X-ray diffraction (XRD, Bruker D8 Discover) with Cu Kα radiation and a differential scanning calorimeter (DSC, NETZSCH 404 F3), respectively. The surface morphologies of the reacted ribbons were studied using scanning electron microscope (SEM, FEI Sirion 200). For nanostructural analyses, the ribbons were thinned carefully by a low-angle (5°) ion milling (GATAN-691) and then examined with a high-resolution transmission electron microscope (TEM, FEI Tecnai G2 F20). Binding states of elements on the surfaces of the ribbons were evaluated by X-ray photoelectron spectroscope (XPS, Thermo ESCALAB 250XI) with a monochromic Al Kα X-ray source ($h\nu$ = 1486.6 eV). The power was 150 W, and the X-ray spot size was 500 μm. The pass energy of the XPS analyzer was set as 20 eV. The base pressure of the analysis chamber was lower than 5×10^{-9} Torr. Synchrotron radiation XRD analysis was conducted on the as-quenched FeSiB and FeSiBPCu ribbons in a transmission geometry using the high-intensity, high-energy monochromatic beam at Sector 15U1 at the Shanghai Synchrotron Radiation Facility (SSRF). The photon energy was 20 keV corresponding to an X-ray wavelength of 0.6199 Å, and the beam size was 4×10 μm^2. The X-ray attenuation length of the samples at 20 keV is ∼25 μm. The detector was set at a distance of 163.8 mm, and CeO_2 was used for calibration. The exposure time was 180 s for each sample and the background scattering from air. The resultant 2D image files were integrated using the Fit2D program to obtain 1D intensity distributions as a function of the wavevector Q.

2.3. Degradation Experiments. MB solution (250 mL, 100 mg/L) was prepared using deionized (DI) water in a 500 mL beaker. The temperature (298 K if not noted) of the solution was maintained using a water bath. The initial pH (pH = 3 if not noted) of the solution was adjusted using 5% H_2SO_4 as well as 1 and 0.1 M NaOH. Ribbons (0.5 g/L) and some H_2O_2 (1 mM if not noted) were added into the solution, which was stirred at a fixed speed during the degradation process. At selected time intervals, 2.5 mL of solution was extracted using a syringe and filtered with a 0.22 μm membrane and then scanned using a UV−vis spectrophotometer (Shimadzu UV-1280) to obtain the absorbance spectrum of the solution. For dye mineralization analysis, the sampled MB solution was analyzed by a

DOI: 10.1021/acsanm.8b01669
ACS Appl. Nano Mater. 2019, 2, 214−227

total organic carbon (TOC) analyzer (Shimadzu, TOC-VCPN). For cyclic tests, the ribbons were extracted from the solution after each degradation experiment and stir-washed using DI water for 20 s before being put into the next reaction batch.

3. RESULTS

3.1. Structural Characterization. *3.1.1. Structural Modulation of Ribbons.* The amorphous nature of the as-quenched FeSiB (FeSiB-aq) and FeSiBPCu (FeSiBPCu-aq) ribbons was confirmed, as only broad humps were found in their XRD curves in Figure 1. To obtain single nanocrystalline and

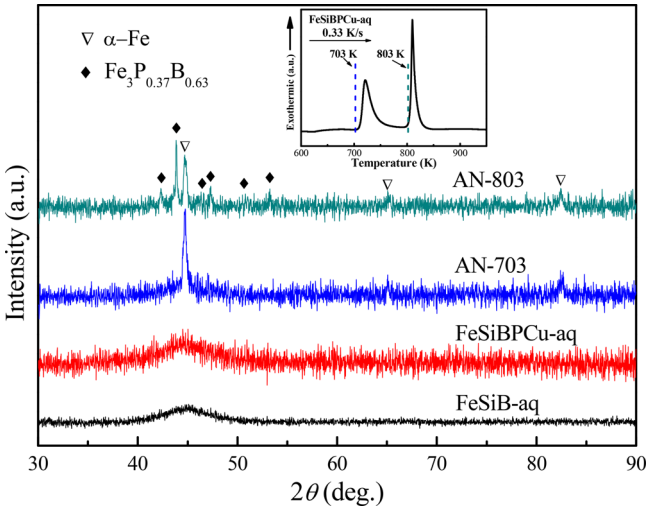

Figure 1. XRD curves of FeSiB-aq, FeSiBPCu-aq, AN-703, and AN-803 ribbons. Inset is the DSC curve of the FeSiBPCu-aq ribbon.

multiple crystalline ribbons, FeSiBPCu-aq ribbons were annealed at different temperatures based on the DSC curve shown in the inset of Figure 1. The FeSiBPCu ribbons annealed at 703 K (AN-703), which is the temperature closest to onset temperature of the first crystallization peak (T_{x1}), consist of α-Fe crystallites in amorphous matrix, while both α-Fe and $Fe_3P_{0.37}B_{0.63}$ grains form in the FeSiBPCu ribbon annealed at 803 K (AN-803), a temperature near the onset temperature of the second crystallization peak (T_{x2}). The average sizes of the crystallites in AN-703 and AN-803 were calculated using the Scherrer equation based on the diffraction peaks at 2θ = 44.7 and 43.8° for α-Fe and $Fe_3P_{0.37}B_{0.63}$ phases, respectively. The average size of α-Fe crystallites in AN-703 ribbon is 22.3 nm, while the α-Fe and $Fe_3P_{0.37}B_{0.63}$ crystallites in AN-803 ribbon are estimated to be 22.9 and 55.1 nm, respectively. The obtained small α-Fe nanocrystallites reveal the effective phase separation by Cu−P atom pairs in FeSiBPCu amorphous ribbons.

3.1.2. Structural Heterogeneity. To unveil nanostructures of the alloys, TEM analyses were performed on thin sections of FeSiB-aq, FeSiBPCu-aq, AN-703, and AN-803 ribbons. As shown in Figure 2(a,b), only homogeneous structures are observed in all the analyzed areas of the FeSiB-aq sample. In addition, as only a blurry ring is present in the selected area diffraction in the inset of Figure 2(a), and no diffraction ring is found in the FFT of the observed area in the inset of Figure 10(b), the homogeneous amorphous structure of FeSiB-aq ribbons can be confirmed. (Multiple areas of the sample have been analyzed without traces of clusters or crystallites found.) In Figure 2(c), both the TEM image and selected area

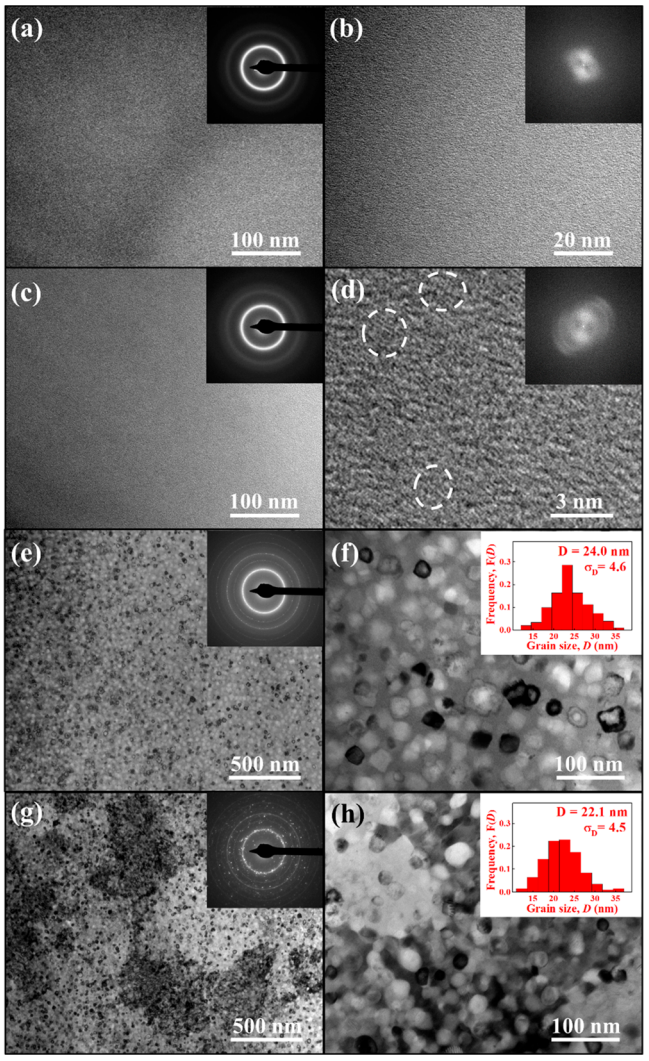

Figure 2. TEM analyses of the (a,b) FeSiB-aq, (c,d) FeSiBPCu-aq, (e,f) AN-703, and (g,h) AN-803 ribbons.

diffraction of the FeSiBPCu-aq sample present characteristics of a homogeneous amorphous structure. However, the high-resolution TEM image and FFT of the investigated area in Figure 2(d) reveal the existence of some short-range ordered clusters, which are about 2−3 nm in size, highlighted by the white dashed ellipses. On the basis of the diffraction lattice and FFT, the structure of the clusters is very close to bcc α-Fe nanocrystal.

A large amount of nanocrystals are present in AN-703 ribbons as shown in Figure 2(e,f). All the rings from the selected area diffraction pattern in the inset of Figure 2(e) are from α-Fe crystallites, which is consistent with XRD results. The average diameter of the nanocrystals is 24.0 nm as shown in the inset of Figure 2(f), which is close to the calculation from XRD results. For AN-803 sample, not only nanocrystals but also crystallites with large diameters are present in the TEM images, as shown in Figure 2(g,h). The nanocrystals are about 22.1 nm in diameter and proved to be α-Fe, while the large crystals that are more than 100 nm in diameter are the $Fe_3P_{0.37}B_{0.63}$ phase. The inconsistent values of the diameters of $Fe_3P_{0.37}B_{0.63}$ crystals between XRD and TEM results are because the Scherrer equation is only applicable for diameter calculation of crystals less than 100 nm.

DOI: 10.1021/acsanm.8b01669
ACS Appl. Nano Mater. 2019, 2, 214−227

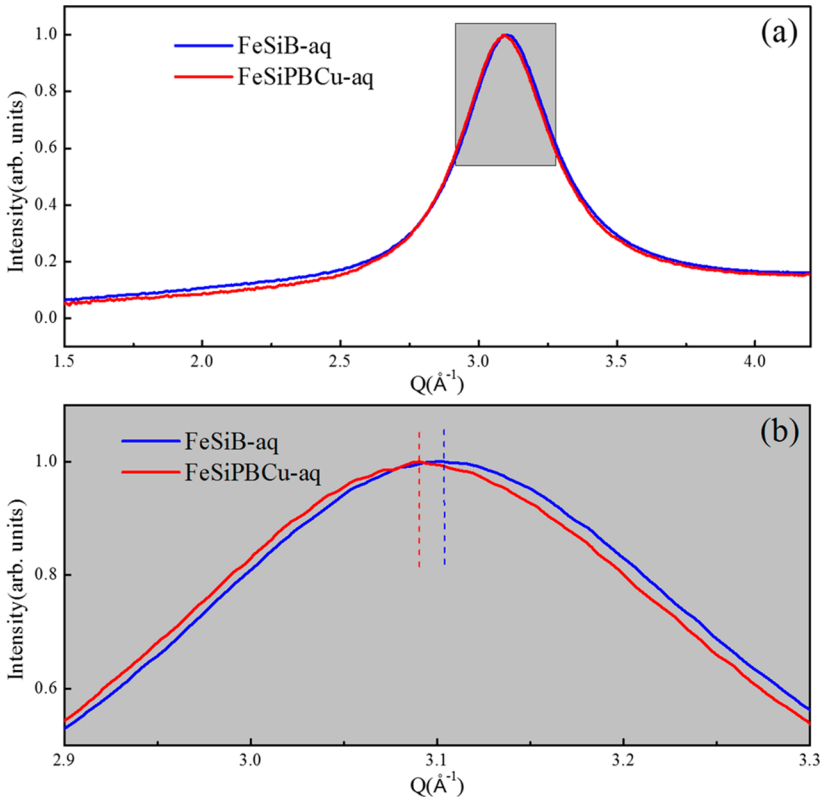

Figure 3. (a) Synchrotron radiation XRD of FeSiB-aq and FeSiBPCu-aq ribbons. (b) Enlarged image of the gray area shown in (a) with dashed lines denoting the peak positions.

Synchrotron radiation XRD was performed on FeSiB-aq and FeSiBPCu-aq ribbons, with the primary diffraction peak shown in Figure 3(a). The gray area in Figure 3(a) is enlarged and shown in Figure 3(b) with dashed lines denoting the peak positions. The Q value of the primary peak (Q1) for FeSiBPCu-aq ribbon is smaller than that for FeSiB-aq ribbon. As Q1 is inversely proportional to the mean atomic spacing,[41] the left shift of Q1 from FeSiB-aq to FeSiBPCu-aq ribbons indicates that the average atomic spacing in FeSiBPCu-aq ribbons is larger than that in FeSiB-aq ribbons, which may come from the impulsive forces between Fe−P and Fe−Cu atomic pairs. The synchrotron XRD results provide evidence about the structural change induced in FeSiB amorphous alloys by minor addition of P and Cu atoms, even though the atomic percentage of P and Cu is low in this work.

3.1.3. Surface Chemical States. The chemical states on the surfaces of alloys can be largely affected by annealing, which in turn changes the reactivities of catalysts. XPS analyses were carried out on the surfaces of FeSiBPCu-aq, AN-703, and AN-803 ribbons over a wide binding energy range, including Fe $2p_{3/2}$, O 1s, Cu 2p, Si 2p, B 1s, and P 2p, to uncover the effect of annealing on the surface chemical states of alloys, as shown in Figure 4. Both metallic iron Fe^0 and ferric ions Fe^{3+} are detected on the surfaces of FeSiBPCu-aq, AN-703, and AN-803 ribbons,[42] while ferrous ions Fe^{2+} only appear on the FeSiBPCu-aq ribbon, as shown in Figure 4(a). This is because Fe^{2+} is metastable and can be oxidized easily with increased temperature during annealing. Both Fe^{2+} and Fe^{3+} are oxidized iron (Fe^{ox}). The amount ratios of Fe^0/Fe^{ox} for FeSiBPCu-aq, AN-703, and AN-803 ribbons are 5.5, 18.2, and 14.1%, respectively. The large amount of crystallized α-Fe in the annealed samples results in the increased Fe^0 percentage on the surface of AN-703 ribbon, while the formed large $Fe_3P_{0.37}B_{0.63}$ crystals in AN-803 ribbon lead to a slight decrease of Fe^0/Fe^{ox}.

All of the peaks from O 1s on the surfaces of the three kinds of ribbons can be deconvoluted into two types of bonds as shown in Figure 4(b), with the peaks at lower binding energy representing Fe−O bonds, and the peaks at higher binding energy representing bonds with metalloid elements (M−O).[43,44] After annealing, the amount ratio of $M-O/O_{total}$ bonds increases as more metalloid elements are oxidized at higher temperatures. As shown in Figure 4(c), metallic copper (Cu^0) and cuprous ions (Cu^+) are present in all the ribbons, while cupric ions (Cu^{2+}), including those from copper hydroxides $Cu(OH)_2$, only appear in AN-703 and AN-803 ribbons.[37,45] On the basis of the results, the annealing treatment promotes further oxidization of Cu^0 and Cu^+.

For metalloid elements, including silicon, boron, and phosphorus, their zero-valent and oxidized states exist on the surfaces of both FeSiBPCu-aq and AN-703 ribbons, while only oxidized states exist on that of the AN-803 ribbon, as shown in Figure 4(d−f).[37,46−48] The amount ratios of Si^{4+}/Si_{total}, B^{3+}/B_{total}, and P^{5+}/P_{total} increase from 0.62, 0.64, and 0.55 in FeSiBPCu-aq to 0.85, 0.79, and 0.66 in AN-703, respectively. All of Si, B, and P were oxidized on the surface of AN-803. It is easier for zero-valent metalloids to get oxidized at higher annealing temperature. B^{3+} mostly comes from B_2O_3, which is soluble in acidic solutions. On the surfaces of Fe-based alloys, P^{5+} usually belongs to iron phosphates, including $FePO_4{\cdot}H_2O$ and $Fe_3(PO_4)_2$, which have very low-solubility products, with K_{sp} ranging from 10^{-36}−10^{-25} at room temperature.[49] Si^{4+} usually comes from SiO_2, which has very low solubility in

DOI: 10.1021/acsanm.8b01669
ACS Appl. Nano Mater. 2019, 2, 214−227

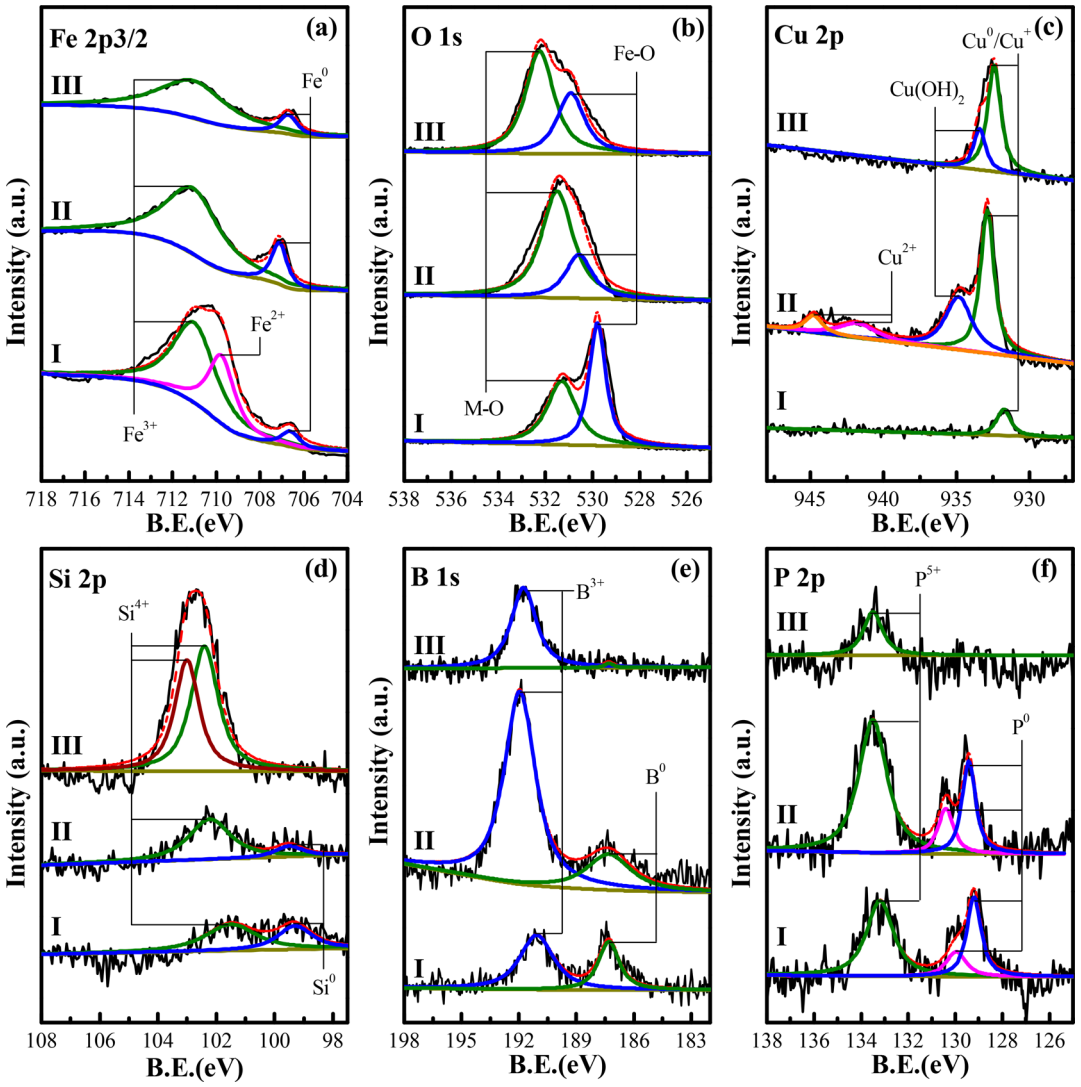

Figure 4. XPS analyses of the binding energies of (a) Fe $2p_{3/2}$, (b) O 1s, (c) Cu 2p, (d) Si 2p, (e) B 1s, and (f) P 2p for the amorphous and annealed FeSiBPCu ribbons (I: FeSiBPCu-aq, II: AN-703, III: AN-803).

acidic solution, as it can even serve as a protective coating for stainless steel in H_2SO_4 solution.[50]

3.2. Catalytic Performance of Ribbons. *3.2.1. Catalytic Performance at Room Temperature.* To obtain the catalytic performances of the ribbons in MB degradation at room temperature, Fenton-like reactions using FeSiBPCu-aq, AN-703, AN-803, and FeSiB-aq ribbons were carried out respectively, with reaction parameters set as T = 298 K, pH = 3, initial concentration of hydrogen peroxide (C_{HP}) = 1 mM, ribbon dosage: 0.5 g/L, and initial concentration of MB solution (C_{MB}) = 100 mg/L. The concentration of filtered MB solution at different reaction times was measured using UV−vis spectroscopy. As shown in Figure 5, four major absorption peaks are observed for MB solutions, with the peaks at 247 and 291 nm representing triazine groups, and the peaks at 618 and 653 nm representing chromophore groups, respectively.[51] The decreased peak values of the absorbance spectra correspond to the reduced MB concentration of the solution with reaction time. The results reveal that the catalytic abilities of both FeSiBPCu-aq ribbons and AN-703 ribbons were better than the widely investigated FeSiB-aq ribbons, while that of AN-803 ribbons was similar to that of FeSiB-aq ribbons.

In order to quantitatively compare catalytic efficiencies of the four kinds of ribbons, the absorbance values of the peak at 653 nm in UV−vis spectra were normalized and plotted in Figure 6(a). C_t is the instant concentration of MB (mg/L), and C_0 is the initial concentration of MB (mg/L). When C_t/C_0 < 5% (95% of MB is decomposed), the degradation is considered to be completed due to instrumental fluctuation in this work. On the basis of the calculation from normalized peak values, it is found that MB disappeared completely within 9 min using both FeSiBPCu-aq and AN-703 ribbons, while the overall time required for MB degradation using FeSiB-aq and AN-803 ribbons was both 12 min. The MB degradation experiment using only H_2O_2 (without Fe-based ribbons) was also carried out, and little change of MB concentration was observed within 18 min. Thus, the disturbing factor from the H_2O_2 degradation effect can be neglected for this work. The degradation kinetics after the first minute are commonly described by a pseudo-first-order equation as given below

$$C_t = C_0 * \exp(-kt) \quad (1)$$

where k is the reaction rate constant (min^{-1}), and t is the reaction time (min). k is defined as the slope of the linear

DOI: 10.1021/acsanm.8b01669
ACS Appl. Nano Mater. 2019, 2, 214−227

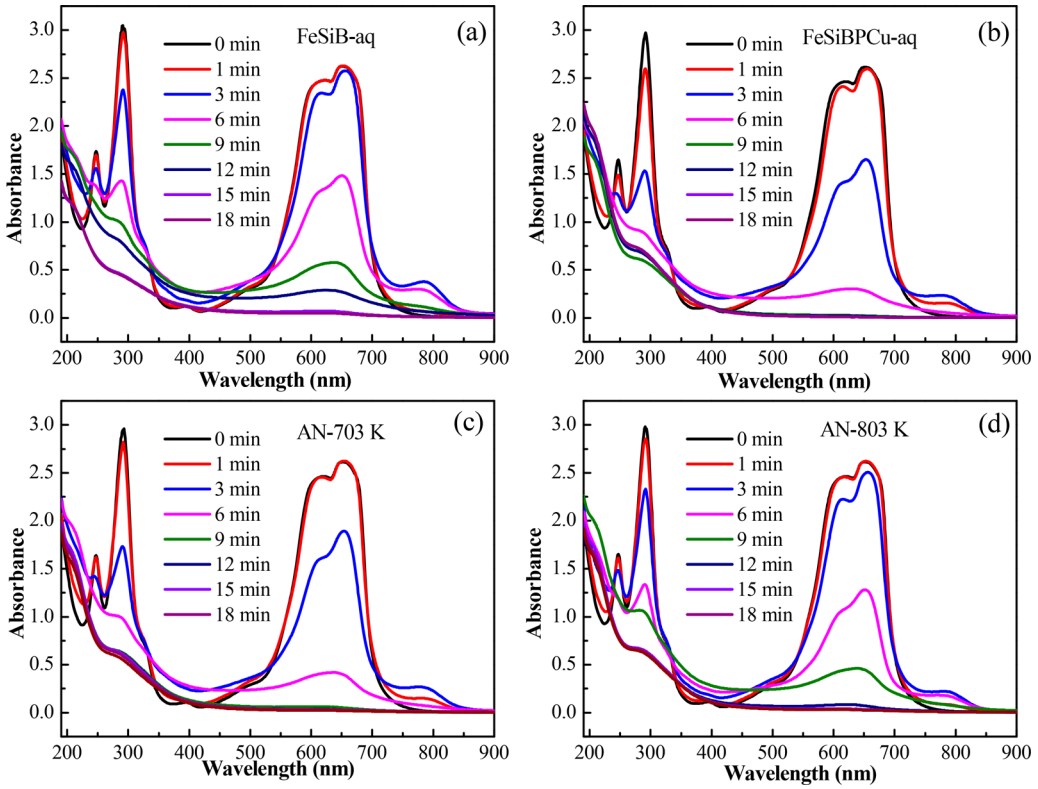

Figure 5. UV−vis absorbance spectra of MB solutions at different times during Fenton-like reactions using (a) FeSiB-a (b) FeSiBPCu-aq, (c) AN-703, and (d) AN-803 ribbons as catalysts (T = 298 K, pH = 3, C_{HP} = 1 mM, ribbon dosage: 0.5 g/L, C_{MB} = 100 mg/L).

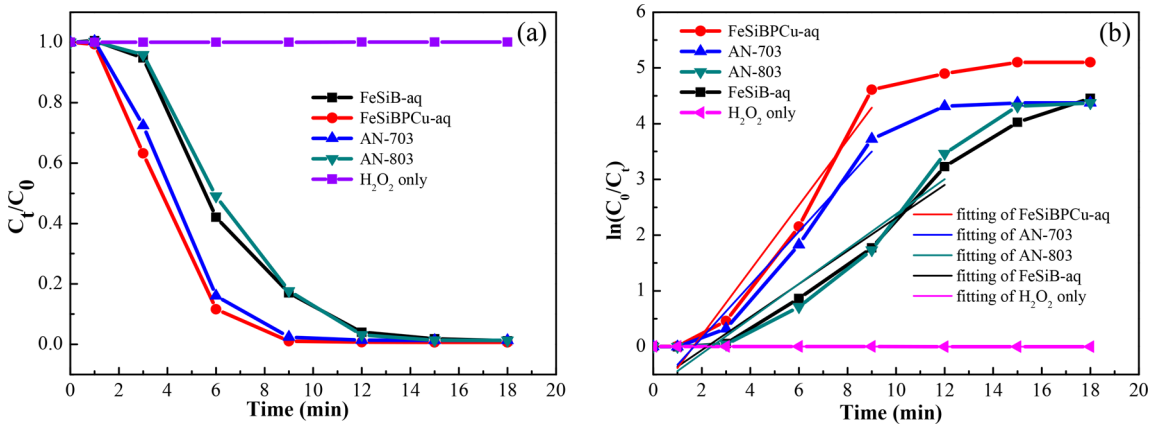

Figure 6. (a) Normalized concentration changes of MB solutions and (b) the $\ln(C_0/C_t)$ vs time curves for the degradation process using FeSiB-aq, FeSiBPCu-aq, AN-703, and AN-803 ribbons as catalysts (T = 298 K, pH = 3, C_{HP} = 1 mM, ribbon dosage: 0.5 g/L, C_{MB} = 100 mg/L).

fitting for $\ln\left(\frac{C_0}{C_t}\right)$ vs time as shown in Figure 6(b). In order to reduce the experimental error from the high absorbance of initial MB solution, the C_t/C_0 values at t = 0 and 1 min were not taken into account for calculation of the reaction constants. On the basis of the linear fitting from the plots, the reaction rate constants using FeSiBPCu-aq, AN-703, AN-803, and FeSiB-aq as catalysts are 0.58, 0.48, 0.31, and 0.30 min^{-1}, respectively. The reaction rate constant of AN-703 is slightly lower than that of FeSiBPCu-aq but still much higher than that of AN-803 or FeSiB-aq ribbons.

The TOC removal using FeSiBPCu-aq ribbons is shown in Figure S1(a). The results reveal that the MB mineralization process requires longer time than breaking the chromophore bonds, as it takes time for byproducts to be decomposed to final products,[51] including H_2O, CO_2, NO_3^-, and SO_4^{2-}. The effect of TBA on MB degradation efficiency was studied, with results shown in Figure S1(b). The sharply decreased dye degradation rate with the addition of TBA clearly verifies the generation of hydroxyl radicals during the Fenton-like reactions in this work.

3.2.2. Change of Surface Morphology. The catalytic efficiencies of amorphous/crystalline ribbons are closely related to their surface morphology change during the decolorization reactions. The loose 3D nanoporous structures have been proven to be beneficial to mass transport and are desirable in high-efficiency catalysts for amorphous/nanocrystalline ribbons.[9] To further evaluate the catalytic performance of the ribbons, surface morphologies of FeSiB-aq,

DOI: 10.1021/acsanm.8b01669
ACS Appl. Nano Mater. 2019, 2, 214−227

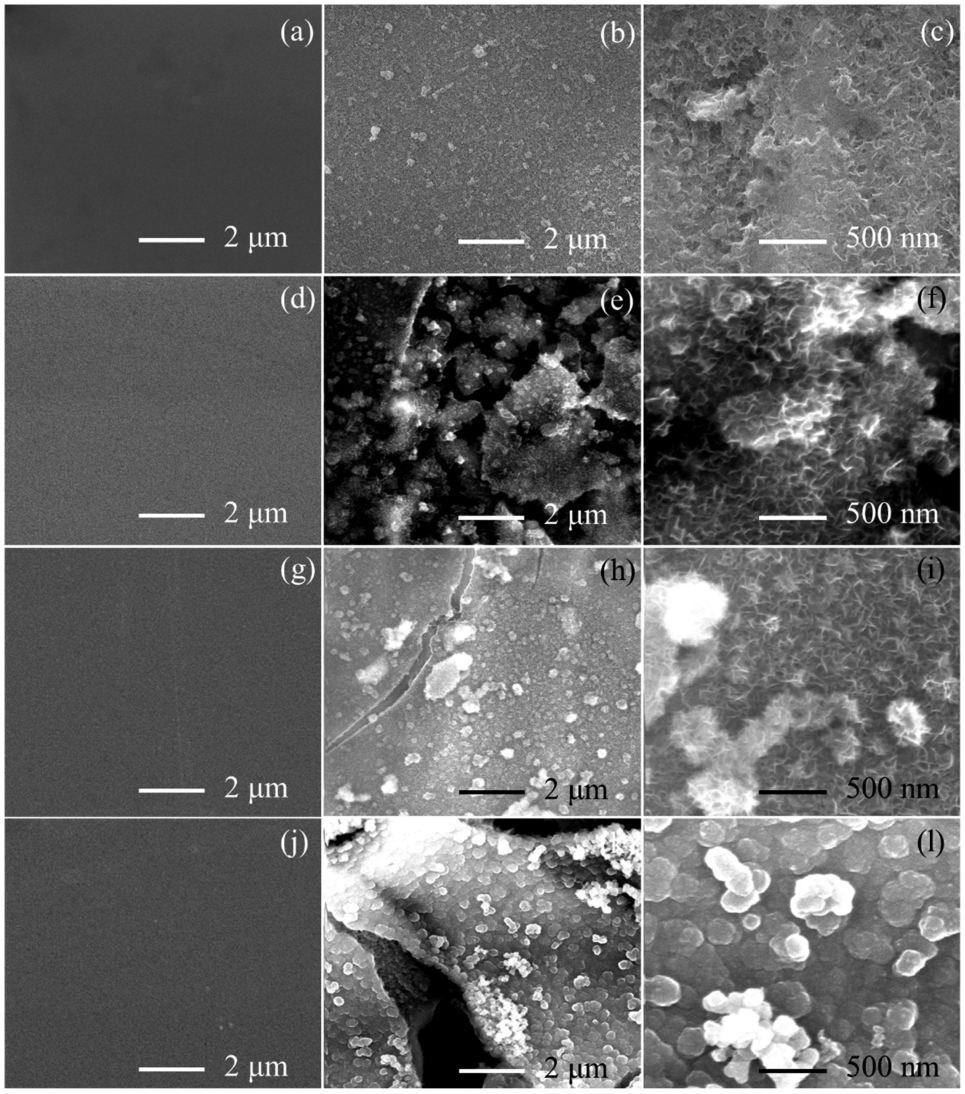

Figure 7. Surface morphology of the unreacted and reacted ribbons analyzed by SEM, including (a) unreacted and (b,c) reacted FeSiB-aq, (d) unreacted and (e,f) reacted FeSiBPCu-aq, (g) unreacted and (h,i) reacted AN-703, and (j) unreacted and (k,l) reacted AN-803.

FeSiBPCu-aq, AN-703, and AN-803 ribbons before and after the degradation experiments were compared using SEM as shown in Figure 7. The surfaces of unreacted FeSiB-aq (Figure 7a), FeSiBPCu-aq (Figure 7d), AN-703 (Figure 7g), and AN-803 (Figure 7j) ribbons are smooth without visible defects.

After the reaction, the surfaces of FeSiB-aq ribbons present a certain amount of 3D nanoporous structures, as shown in Figure 7(b) and the enlarged image in Figure 7(c). However, the density of the pores is low, and the penetration is not satisfactory for intense mass transfer. On the other hand, the reacted surface layers of FeSiBPCu-aq [Figure 7(e,f)] and AN-703 ribbons [Figure 7(h,i)] are covered with loose 3D nanoporous structures, which are typically characteristic of highly efficient catalysts. For AN-803 ribbons, no porous structure is observed on the surface after the degradation experiment. Instead, the surface is covered with densely packed particles, which can separate the underneath part from the dye solution. The densely packed surface morphology formed during the reaction is one of the reasons for the low catalytic efficiency of AN-803 ribbons.

3.2.3. Reaction Activation Energy. The influence of temperature on catalytic efficiencies of FeSiBPCu-aq, AN-703, AN-803, and FeSiB-aq ribbons in Fenton-like reactions was analyzed by carrying out the degradation experiments at 308, 318, and 328 K. The degradation results at 298 K are also plotted here for comparison as shown in Figure 8. The reaction conditions were set as initial pH = 3, C_{HP} = 1 mM, ribbon dosage: 0.5 g/L, and C_{MB} = 100 mg/L. At 308 K, MB solutions were completely decolorized in the reactions using FeSiBPCu-aq, AN-703, AN-803, and FeSiB-aq ribbons within 6, 6, 9, and 9 min, respectively. At 318 K, those processes finished within 3, 6, 6, and 6 min, respectively. At 328 K, all of the processes finished within 3 min. For all the catalysts, the decolorization processes took less time with increased solution temperature, revealing the positive influence of temperature on degradation. Raising temperature accelerates the Fenton reaction process, which increases the generation rate of ·OH and the decolorization efficiency.[52,53]

The reaction rate constants at different temperatures for the solutions using the four kinds of catalysts are summarized in Figure 9(a). When the solution temperature increases from 298 to 308, 318, and 328 K, the degradation rate constant of FeSiBPCu-aq ribbons increases from 0.58 to 0.79, 1.78, and 1.55 min^{-1}, that of AN-703 ribbons increases from 0.48 to

DOI: 10.1021/acsanm.8b01669
ACS Appl. Nano Mater. 2019, 2, 214−227

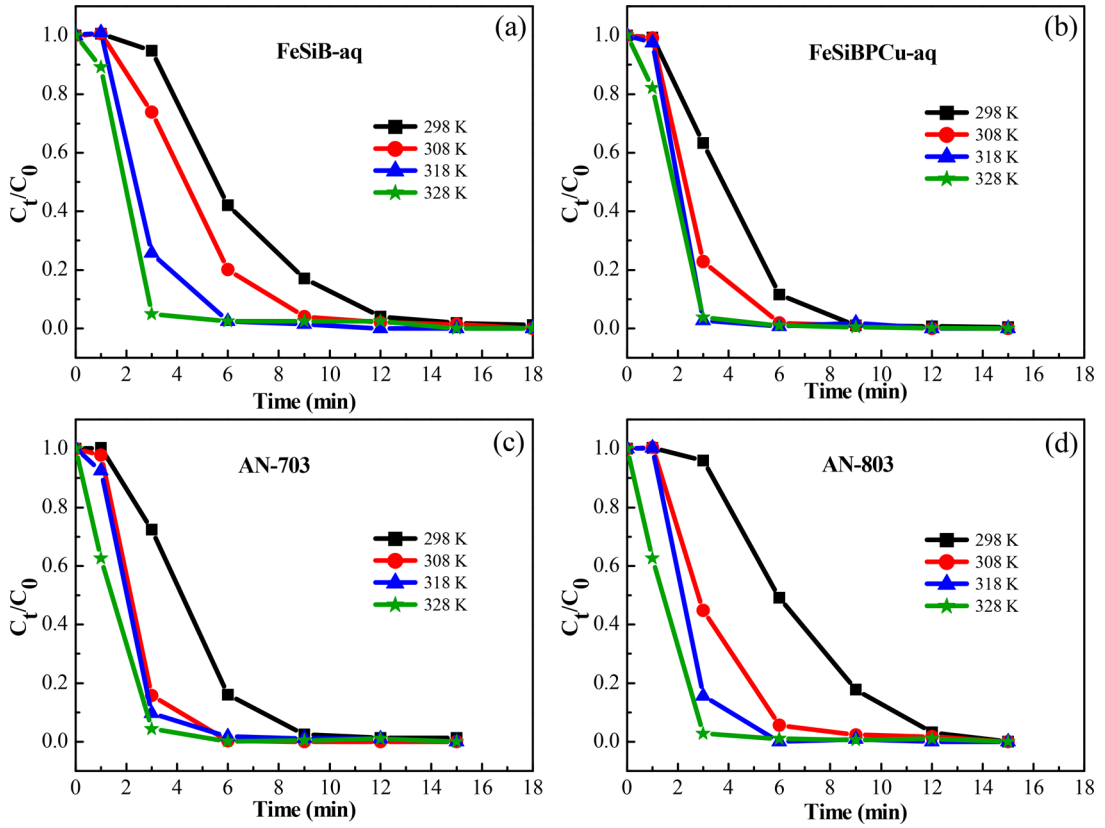

Figure 8. Normalized concentration changes of MB solutions during the Fenton-like reactions using (a) FeSiB-aq, (b) FeSiBPCu-aq, (c) AN-703, and (d) AN-803 ribbons as catalysts at different temperatures (pH = 3, C_{HP} = 1 mM, ribbon dosage: 0.5 g/L, C_{MB} = 100 mg/L).

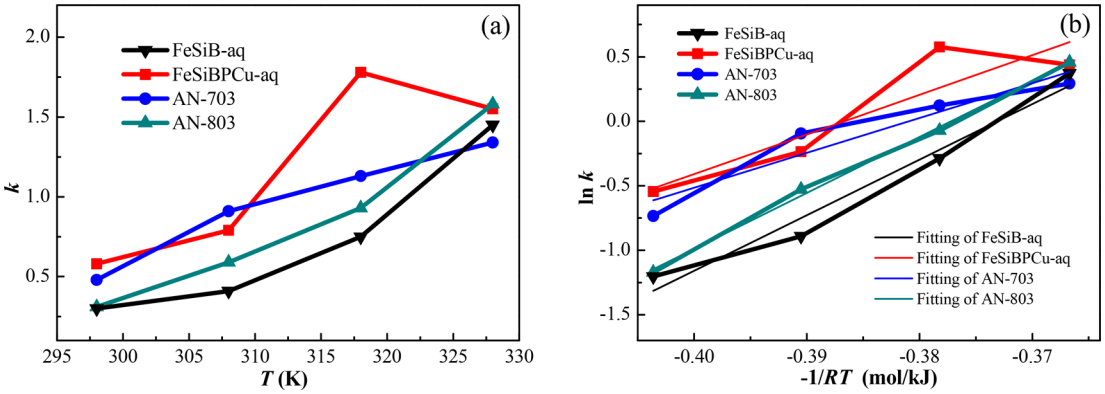

Figure 9. (a) Derived reaction rate constants k and (b) ln k vs $-1/RT$ curves for the degradation processes using FeSiB-aq, FeSiBPCu-aq, AN-703, and AN-803 ribbons at different reaction temperatures (pH = 3, C_{HP} = 1 mM, ribbon dosage: 0.5 g/L, C_{MB} = 100 mg/L).

0.91, 1.13, and 1.34 min^{-1}, that of AN-803 increases from 0.31 to 0.59, 0.93, and 1.58 min^{-1}, and that of FeSiB-aq increases from 0.30 to 0.41, 0.75, and 1.45 min^{-1}, respectively. Most of the reaction rate constants increased with the raised reaction temperature, except for a slight decrease of k values from 318 to 328 K using the FeSiBPCu-aq ribbon. This may be because the degrading reactions using FeSiBPCu-aq ribbons at 328 K finish so fast that our experimental setup is not sensitive enough to accurately determine its reaction rate constant.

As reaction rate is highly affected by temperature, we can derive the thermal activation energy for MB degradation in Fenton-like reactions using the ribbons by the Arrhenius-type equation

$$\ln k_T = -\frac{\Delta E}{RT} + \ln A \quad (2)$$

where k_T is the reaction rate constant at different temperatures, ΔE is the reaction activation energy, R is the gas constant, and A is a constant. The ln k_T vs $-1/RT$ plots are shown in Figure 9(b), with the reaction activation energies of the solutions using FeSiBPCu-aq, AN-703, AN-803, and FeSiB-aq ribbons being 31, 27, 43, and 43 kJ/mol, respectively. FeSiBPCu-aq and AN-703 ribbons have similar reaction activation energies, which are lower than those of AN-803 and FeSiB-aq, revealing that FeSiBPCu-aq and AN-703 ribbons are more effective catalysts compared with AN-803 and FeSiB-aq ribbons. As the reaction activation energy using the four kinds of ribbons is lower than that of an ordinary reaction, 60−250 kJ/mol, the

DOI: 10.1021/acsanm.8b01669
ACS Appl. Nano Mater. 2019, 2, 214−227

catalytic abilities of all the ribbons prepared in this work can be confirmed.[54,55]

3.3. Influences of Reaction Parameters. According to the process of Fenton-like reactions,[56] four parameters influence the efficiency of catalysts for dye degradation, including pH, initial H_2O_2 concentration, dye concentration, and catalyst dosage. As reported before, catalytic efficiency is always improved with reduced dye concentration and increased ribbon dosage, while both pH range and H_2O_2 concentration have optimum conditions for Fenton-like reactions.[29,57] According to the Fenton-like reactions carried out under different pHs and initial H_2O_2 concentrations using the four kinds of ribbons as shown in Figures S2 and S3, all four kinds of catalysts have the best catalytic performance at pH = 3 or when the initial H_2O_2 concentration is 5 mM.

3.4. Reusability of FeSiBPCu-aq Ribbons. Other than catalytic efficiency, reusability of catalysts is also an important factor for industrial application. Considering the catalytic efficiency and preparation cost simultaneously, the FeSiBPCu-aq ribbon is the most suitable catalyst for Fenton-like reaction. Thus, cyclic tests were carried out on FeSiBPCu-aq ribbons with experimental parameters set as T = 298 K, initial pH = 3, C_{HP} = 1 mM, ribbon dosage: 0.5 g/L, and C_{MB}= 100 mg/L. The normalized concentrations of MB with reaction time as well as the time required for the completion ($t_{95\%}$) of each reaction cycle are presented in Figure 10(a) and (b), respectively. The ribbons in the first and second cycles had similar catalytic performances, as the reactions both finished within 9 min. The reaction completion time increased linearly from the 3rd to 6th reaction cycles reaching 25 min and stayed constantly from the 6th to 15th cycles. It took each reaction from the 16th to 20th cycles 30 min to finish. The ribbons still showed satisfying catalytic ability when the experiments were dropped after 20 reaction cycles, revealing the long service life of FeSiBPCu-aq ribbons.

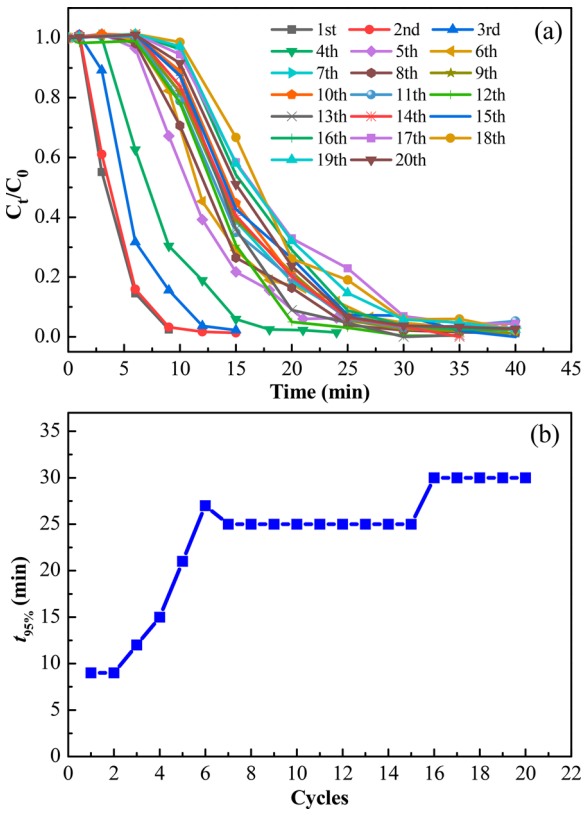

Figure 10. (a) Normalized concentration changes of MB solutions and (b) times required for 95% completion of the degradation process vs reaction cycles for the Fenton-like reactions using FeSiBPCu-aq catalysts from the 1st to the 20th degradation cycles.

4. DISCUSSION

4.1. Competitive Effects of Structural Heterogeneity and Surface Chemical States on Catalytic Performance. On the basis of catalytic performance analyses of the ribbons, both FeSiBPCu amorphous and single nanocrystalline ribbons show higher catalytic efficiencies for Fenton-like reactions than the widely investigated FeSiB amorphous ribbons, while FeSiBPCu multiple crystalline ribbons have lower catalytic ability. Origins of the different catalytic performances of ribbons are related to their nanostructures, which affect the reactivity of Fe atoms as well as surface chemistry, because Fenton-like reactions are surface-mediated.

For FeSiBPCu-aq ribbons, the heterogeneous structures in this alloy come from the large positive mixing enthalpy between Fe atoms and Cu−P pairs, which promotes the formation of α-Fe clusters in Fe-rich regions. The heterogeneous structures in Fe-based amorphous alloys can form galvanic cells and improve the catalytic performance of the alloy during electrochemical processes. Besides, not many passive films can be formed on the surfaces of FeSiBPCu-aq ribbons, as most of the metalloid elements are in their zero-valent states. This explains the higher catalytic efficiency of FeSiBPCu-aq than FeSiB-aq and AN-803 ribbons.

AC-703 ribbons have a large amount of α-Fe nanocrystals dispersed evenly in amorphous matrix based on the TEM results in Figure 2. It was reported that the composition of the residue amorphous phase in the FeSiBPCu nanocrystalline alloy is close to $Fe_{76}Si_9B_{10}P_5$, which is electrochemically more stable than α-Fe.[58] A larger number of galvanic cell structures can be formed between α-Fe nanocrystals and amorphous matrix in AN-703 ribbons than in FeSiBPCu-aq ribbons. In addition, more Fe^0 is available on the surfaces of AC-703 ribbons because of the formation of massive α-Fe nanocrystals. Thus, AN-703 ribbons should have better catalytic performance than FeSiBPCu-aq ribbons. However, Fenton-like reactions using FeSiBPCu-aq and AN-703 ribbons under the same reaction conditions both finished within the same amount of time. The k value of the reactions using AN-703 even decreased slightly, which is consistent with the reported results.[36] According to XPS analyses, the amount ratio of oxidation states for all the metalloid elements, including B, Si, and P, increased with annealing. The relative amounts of B^{3+}, Si^{4+}, and P^{5+} on the surface of AN-703 are more than those on the surface of the FeSiBPCu-aq ribbon. The enrichment of low-solubility iron phosphates and silica on the surface of AN-703 ribbon decreases the mass and electron transfer rate for the degradation process. Thus, for AN-703 ribbon, the competition between the positive factors (the large amount of galvanic cells formed between α-Fe and amorphous matrix as well as the increased amount of Fe^0 on the surface) and the negative factor (formation of corrosion-resistant iron phosphate and silica layer on the surface) makes its catalytic performance the same as for the FeSiBPCu-aq ribbon.

For AN-803 ribbons, not only α-Fe nanocrystals but also large $Fe_3P_{0.37}B_{0.63}$ crystals exist in amorphous matrix. Galvanic cell structures can form between α-Fe and $Fe_3P_{0.37}B_{0.63}$, α-Fe

DOI: 10.1021/acsanm.8b01669
ACS Appl. Nano Mater. 2019, 2, 214−227

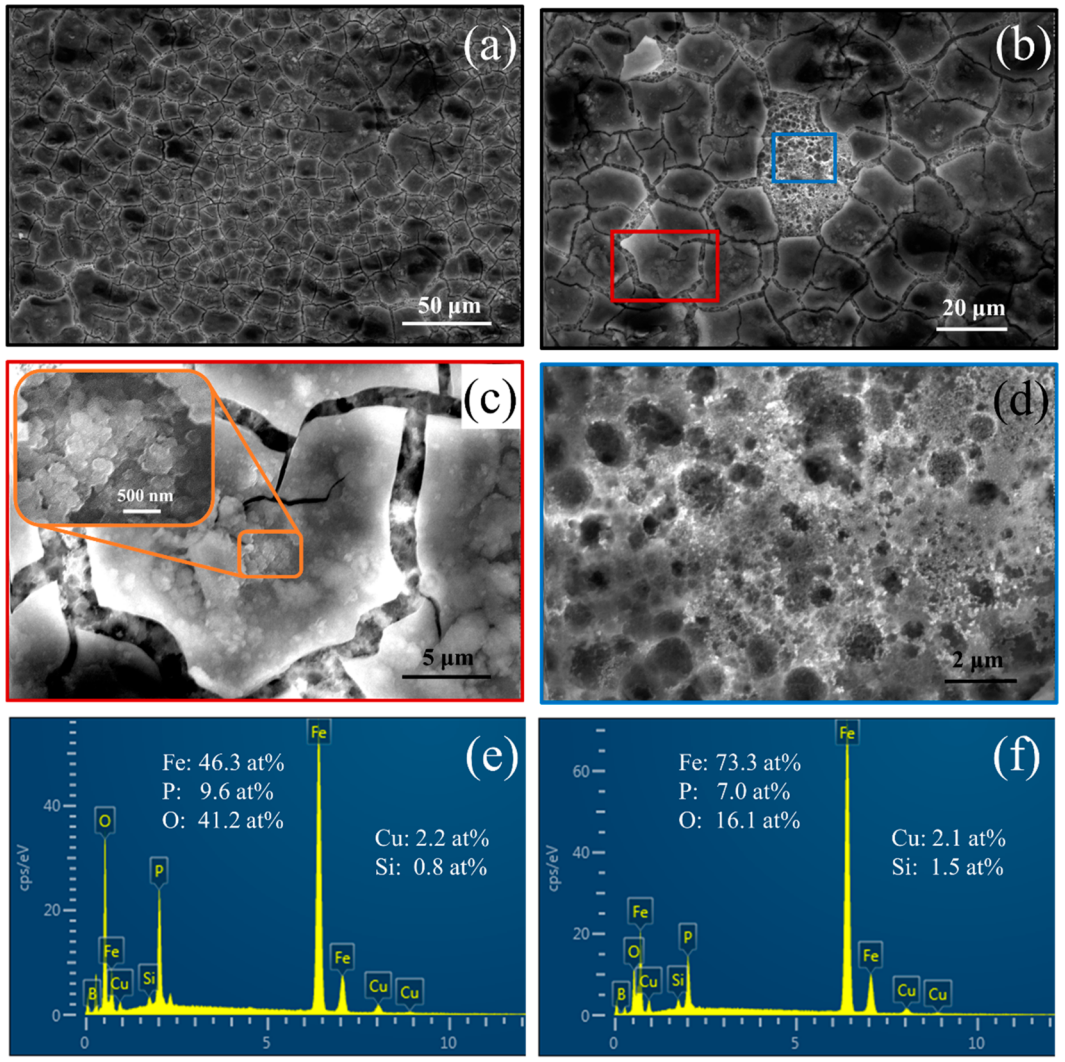

Figure 11. Surface morphologies of FeSiBPCu-aq ribbons after 20 degradation cycles: (a) cracked passive films covering the whole surface; (b) representative areas of passive film and underlying matrix indicated by red square and blue square; the enlarged surface morphologies of (c) passive film and (d) underlying matrix; EDS analysis of the (e) passive film and (f) underlying matrix.

and amorphous matrix, as well as $Fe_3P_{0.37}B_{0.63}$ and amorphous matrix. Although some work found that Fe-based nanocrystalline ribbons with multiple crystalline phases depositing in amorphous matrix showed higher chemical reactivity than their pure amorphous counterparts, AN-803 ribbons with two crystalline phases showed lower catalytic efficiency than FeSiBPCu-aq or AN-703 ribbons in this work. The $Fe_3P_{0.37}B_{0.63}$ large crystals increase the stability of AN-803 ribbons and consume a large amount of Fe^0, both of which depress the reaction activity of the sample. Also, most of the metalloid elements on the surface of AN-803 are oxidized, which leads to the formation of corrosion-resistant silica and an iron phosphate surface layer that impede mass and electron transfer for Fenton-like reactions. This may also explain the stable passive films formed on the surface of a reacted AN-803 ribbon. As a result, the low catalytic efficiency of the AN-803 ribbon can be attributed to the dominated negative factors induced by annealing, including the stable intermetallic compound formed in AN-803 as well as the reduced amount of Fe^0 and the enrichment of silica and iron phosphates with excellent corrosion resistance on the surface, in spite of the large amount of galvanic cells formed among α-Fe, $Fe_3P_{0.37}B_{0.63}$, and amorphous matrix.

The change of surface chemical states and structural heterogeneity during annealing highly depends on the composition of amorphous alloy as well as the annealing process. With different amounts of metallic and metalloid elements in amorphous alloys, the obtained nanocrystalline alloys may have different amount/types of crystalline phases, which lead to different surface reactivities. Even for the alloys with the same composition, a variation of the thermodynamics and kinetics of the annealing process can also result in a tremendous change of the composition on the surface and structure inside the obtained crystalline alloys. This should explain the contrary results in different reported works regarding the effect of annealing on the chemical reactivity of Fe-based amorphous ribbons. When the influence of structural heterogeneity dominates, the nanocrystalline alloys have better chemical reactivity than amorphous alloys; when the influence of surface passivation dominates, the reactivity of amorphous alloys can be reduced through annealing treatment.

4.2. Origin of Long Service Life. FeSiBPCu-aq ribbons not only have high catalytic efficiency in Fenton-like reactions

DOI: 10.1021/acsanm.8b01669
ACS Appl. Nano Mater. 2019, 2, 214−227

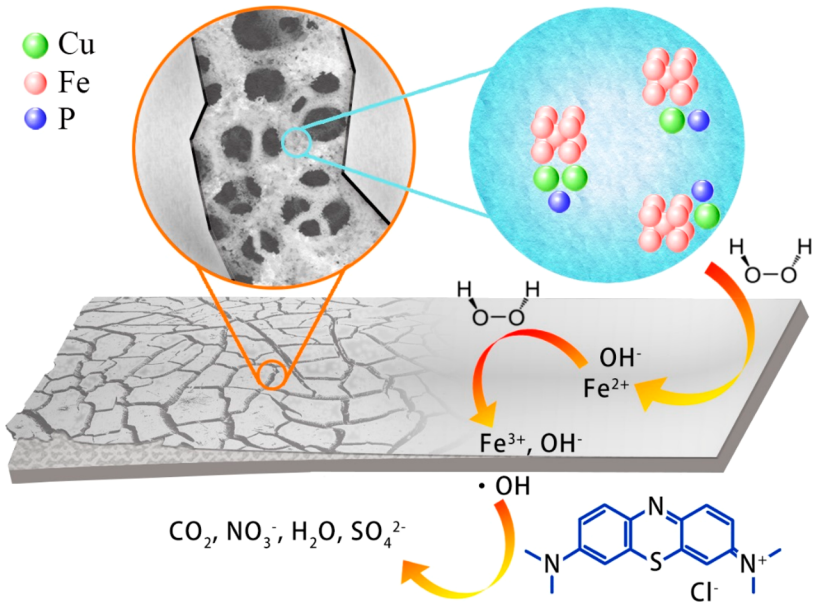

Figure 12. Schematic diagrams of the reaction process of the Fenton-like reaction using FeSiBPCu-aq ribbons.

but also show long service life of more than 20 cycles. In order to unveil the origin of its long service life, the surface morphology of the FeSiBPCu-aq ribbon after 20 cycles was analyzed using SEM and presented in Figure 11. The surface of the reacted ribbon is covered with a large amount of cracked passive film as shown in Figure 11(a), with some pieces of compact film falling off, leaving the underlying matrix exposed [Figure 11(b)]. Morphological details of the areas in the compact film (red square) and the underlying matrix (blue square) are presented in Figure 11(c) and (d), and the elemental compositions of these two areas were analyzed by EDS and shown in Figure 11(e) and (f), respectively. The passive films are made of aggregates of closely packed particles, while multiscale corrosion holes are found on the exposed matrix. Although boron molecules were detected under EDS in both areas, their molecular weight is too light to be accurately measured. The obtained atomic percentages of other elements in Figure 11(e) and (f) were calculated without taking boron content into account. The elemental composition of the porous matrix is close to the nominal content of the FeSiBPCu-aq ribbon, revealing that its surface is newly exposed. Little variation is found for the contents of silicon or copper in the compact film or underlying matrix, while higher amounts of oxygen and phosphorus, as well as a lower amount of iron, were detected on the compact film than on the exposed porous matrix. Thus, it is reasonable to speculate that the top layer of the ribbon surface after 20 reaction cycles is passivated with not only iron oxides but also iron phosphates, which have low solubility even in acidic solutions.[49] The cracks in the passive film come from the released internal stress of the film, as the density of the formed iron oxides and iron phosphates is different from the original amorphous alloy. The deactivation of FeSiBPCu-aq ribbons from the third to sixth reaction cycles results from the formed oxidation layer on the surfaces of ribbons that impede the absorption of dye molecules, which is similar to what was found in previous work.[56,59] The relatively stable reaction rate after the sixth cycle is because of the continuous formation of cracks and shedding of the broken oxidation layer. The cracks on the passive films allow the underlying alloy to get exposed to dye solution and the ribbon to function well as an effective catalyst continuously. On the basis of the above analyses, 4 stages during the 20 recycle tests can be summarized: (i) high degradation efficiency with fresh amorphous ribbon surface from cycles 1–2; (ii) rapidly decreased degradation efficiency from cycles 3–6 because of the decreased amount of Fe^0 on the surface as well as the formed passive films; (iii) fixed reaction rate from cycles 6–15 as the cracks start to form in the passive film, leaving fresh underlying matrix exposed to the dye solution; (iv) slightly decreased reaction rate because of the continuing consumption of the Fe^0 from the explored underlying matrix from cycles 16–20. Methods including vortex-stirring and ultrasonic vibration between cycles to remove oxidation films[13,30,59] as well as modification of alloy composition to eliminate formation of oxidation films[51] can be adopted to improve the stabilities of ribbons in future work.

4.3. Reaction Process Using FeSiBPCu-aq Ribbons.

On the basis of the results and discussion presented above, a schematic diagram of the reaction process of FeSiBPCu-aq ribbons is drawn in Figure 12. The Cu–P pairs induce chemical heterogeneity including iron-rich and iron-poor regions in FeSiBPCu amorphous alloys. α-Fe clusters tend to appear in the iron-rich regions, which are usually next to Cu–P pairs. Galvanic cell structures form between α-Fe clusters and amorphous matrix and accelerate the electron donation rate from Fe^0 in the ribbon. 3D nanoporous structures formed during the first several reaction cycles provide a mass and electron transport pathway for the following degradation reactions. After Fe^0 on the top layer is mostly consumed, the ribbon surface starts to crack because of the stress induced during corrosion, which leaves the underlying surface exposed to the solution and lets the ribbon function continuously as an efficient catalyst.

5. CONCLUSIONS

In this work, the catalytic performances of FeSiBPCu-aq, AN-703, and AN-803 ribbons in Fenton-like reactions were investigated and compared with those of FeSiB-aq ribbons. On the basis of the analyses of catalytic performance, surface

DOI: 10.1021/acsanm.8b01669
ACS Appl. Nano Mater. 2019, 2, 214–227

morphology, and reaction activation energy, FeSiBPCu-aq and AN-703 ribbons have better catalytic ability than FeSiB-aq and AN-803 ribbons. The catalytic performance of ribbons is proposed to be determined by competitive effects of structural heterogeneity and surface chemical states. The galvanic cells formed between amorphous matrix and α-Fe clusters, which was induced by the positive mixing enthalpy between Fe and Cu−P pairs in FeSiBPCu-aq ribbons, improves their catalytic ability. The iron phosphate and silica layer with good corrosion resistance formed on the surfaces of AN-703 ribbons makes their catalytic performance the same as FeSiBPCu-aq ribbons, although they have more Fe^0 on the surface and more galvanic cell structures formed between α-Fe nanocrystals and amorphous matrix than the as-quenched ribbons. Formation of stable intermetallic compound $Fe_3P_{0.37}B_{0.63}$ and enrichment of iron phosphates and silica on the surface reduces the catalytic efficiency of AN-803 ribbons.

Influence of reaction parameters on catalytic efficiency of the ribbons was also studied. The highest catalytic efficiency of the ribbons was achieved at pH = 3 and an initial H_2O_2 concentration = 5 mM. Alignment of catalytic performance of the ribbons with their production cost, FeSiBPCu-aq ribbon is the most suitable catalyst for industrial application. FeSiBPCu-aq ribbons show excellent reusability, as the dye degrading process finishes within 30 min even after 20 recycles of using these ribbons as catalysts. The continuous exposure of the underlying alloy matrix to the solution through the cracks formed on the oxidation layer explains the long service life of FeSiBPCu-aq ribbons. This work clarifies the effect of annealing on the catalytic performance of FeSiBPCu amorphous ribbons.

■ ASSOCIATED CONTENT

Supporting Information

The Supporting Information is available free of charge on the ACS Publications website at DOI: 10.1021/acsanm.8b01669.

S1. Dye mineralization and generation of hydroxyl radicals; S2. Influences of reaction parameters, including (S2.1) initial pH value and (S2.2) H_2O_2; supporting figures as described in the text (PDF)

■ AUTHOR INFORMATION

Corresponding Author

*E-mail: blshen@seu.edu.cn (B.S.)

ORCID

Baolong Shen: 0000-0002-0358-6540

Author Contributions

The manuscript was written through contributions of all authors. All authors have given approval to the final version of the manuscript.

Funding

This work was supported by the National Natural Science Foundation of China (Grant Nos. 51631003, 51501037, 51771054, and 51871054), the National Key Research and Development Program of China (Grant No. 2016YFB0300500), and the Fundamental Research Funds for the Central Universities (Grant No. 2242018K40110).

Notes

The authors declare no competing financial interest.

■ ACKNOWLEDGMENTS

The synchrotron radiation XRD was performed at beamline 15U of the Shanghai Synchrotron Radiation Facility (SSRF).

■ REFERENCES

(1) Kanel, S. R.; Manning, B.; Charlet, L.; Choi, H. Removal of arsenic(III) from groundwater by nanoscale zero-valent iron. *Environ. Sci. Technol.* **2005**, *39* (5), 1291−1298.

(2) ElShafei, G. M. S.; Yehia, F. Z.; Eshaq, G.; ElMetwally, A. E. Enhanced degradation of nonylphenol at neutral pH by ultrasonic assisted-heterogeneous Fenton using nano zero valent metals. *Sep. Purif. Technol.* **2017**, *178*, 122−129.

(3) Yoon, I. H.; Kim, K. W.; Bang, S.; Kim, M. G. Reduction and adsorption mechanisms of selenate by zero-valent iron and related iron corrosion. *Appl. Catal., B* **2011**, *104* (1−2), 185−192.

(4) Liu, P.; Zhang, J. L.; Zha, M. Q.; Shek, C. H. Synthesis of an Fe Rich Amorphous Structure with a Catalytic Effect To Rapidly Decolorize Azo Dye at Room Temperature. *ACS Appl. Mater. Interfaces* **2014**, *6* (8), 5500−5505.

(5) Theofanidis, S. A.; Galvita, V. V.; Poelman, H.; Marin, G. B. Enhanced Carbon-Resistant Dry Reforming Fe-Ni Catalyst: Role of Fe. *ACS Catal.* **2015**, *5* (5), 3028−3039.

(6) Bai, S. X.; Huang, B. L.; Shao, Q.; Huang, X. Q. Universal Strategy for Ultrathin Pt-M (M = Fe, Co, Ni) Nanowires for Efficient Catalytic Hydrogen Generation. *ACS Appl. Mater. Interfaces* **2018**, *10* (26), 22257−22263.

(7) Zhang, C. Q.; Zhang, H. F.; Lv, M. Q.; Hu, Z. Q. Decolorization of azo dye solution by Fe-Mo-Si-B amorphous alloy. *J. Non-Cryst. Solids* **2010**, *356* (33−34), 1703−1706.

(8) Zhang, C. Q.; Sun, Q. L. Annealing-induced different decolorization performances of Fe-Mo-Si-B amorphous alloys. *J. Non-Cryst. Solids* **2017**, *470*, 93−98.

(9) Wang, J. Q.; Liu, Y. H.; Chen, M. W.; Xie, G. Q.; Louzguine-Luzgin, D. V.; Inoue, A.; Perepezko, J. H. Rapid Degradation of Azo Dye by Fe-Based Metallic Glass Powder. *Adv. Funct. Mater.* **2012**, *22* (12), 2567−2570.

(10) Li, X. Z.; Pan, Y.; Wu, J. L.; Lu, T.; Wang, N. Efficient photodecomposition of rhodamine B by an Fe-based metallic glass in an oxalic acid solution. *RSC Adv.* **2016**, *6* (95), 92411−92416.

(11) Yang, J. F.; Bian, X. F.; Bai, Y. W.; Lv, X. Q.; Wang, P. Rapid organism degradation function of Fe-based alloys in high concentration wastewater. *J. Non-Cryst. Solids* **2012**, *358* (18−19), 2571−2574.

(12) Xie, S. H.; Huang, P.; Kruzic, J. J.; Zeng, X. R.; Qian, H. X. A highly efficient degradation mechanism of methyl orange using Fe-based metallic glass powders. *Sci. Rep.* **2016**, *6*, 21947.

(13) Chen, S. Q.; Yang, G. N.; Luo, S. T.; Yin, S. J.; Jia, J. L.; Li, Z.; Gao, S. G.; Shao, Y.; Yao, K. F. Unexpected high performance of Fe-based nanocrystallized ribbons for azo dye decomposition. *J. Mater. Chem. A* **2017**, *5* (27), 14230−14240.

(14) Liang, S. X.; Jia, Z.; Zhang, W. C.; Li, X. F.; Wang, W. M.; Lin, H. C.; Zhang, L. C. Ultrafast activation efficiency of three peroxides by $Fe_{78}Si_9B_{13}$ metallic glass under photo-enhanced catalytic oxidation: A comparative study. *Appl. Catal., B* **2018**, *221*, 108−118.

(15) Deng, Z.; Zhang, X. H.; Chan, K. C.; Liu, L.; Li, T. Fe-based metallic glass catalyst with nanoporous surface for azo dye degradation. *Chemosphere* **2017**, *174*, 76−81.

(16) Zhang, H. Y.; Feng, Y. P.; Cheng, Y. Y.; Baro, M. D.; Altube, A.; Garcia-Lecina, E.; Alcaide, F.; Pellicer, E.; Zhang, T.; Sort, J. Nanoporous Fe-Based Alloy Prepared by Selective Dissolution: An Effective Fenton Catalyst for Water Remediation. *Acs Omega* **2017**, *2* (2), 653−662.

(17) Zhang, C. Q.; Sun, Q. L.; Liu, K. G. From adsorption to reductive degradation: Different decolorization properties of metallic glasses based on different iron-group elements. *J. Alloys Compd.* **2018**, *741*, 1040−1047.

(18) Jia, Z.; Duan, X. G.; Qin, P.; Zhang, W. C.; Wang, W. M.; Yang, C.; Sun, H. Q.; Wang, S. B.; Zhang, L. C. Disordered Atomic Packing

DOI: 10.1021/acsanm.8b01669
ACS Appl. Nano Mater. 2019, 2, 214−227

Structure of Metallic Glass: Toward Ultrafast Hydroxyl Radicals Production Rate and Strong Electron Transfer Ability in Catalytic Performance. *Adv. Funct. Mater.* **2017**, *27* (38), 1702258.
(19) Qin, X. D.; Zhu, Z. W.; Liu, G.; Fu, H. M.; Zhang, H. W.; Wang, A. M.; Li, H.; Zhang, H. F. Ultrafast degradation of azo dyes catalyzed by cobalt-based metallic glass. *Sci. Rep.* **2016**, *5*, 18226.
(20) Sha, Y. Y.; Mathew, I.; Cui, Q. Z.; Clay, M.; Gao, F.; Zhang, X. J.; Gu, Z. Y. Rapid degradation of azo dye methyl orange using hollow cobalt nanoparticles. *Chemosphere* **2016**, *144*, 1530−1535.
(21) Wang, J. Q.; Liu, Y. H.; Chen, M. W.; Louzguine-Luzgin, D. V.; Inoue, A.; Perepezko, J. H. Excellent capability in degrading azo dyes by MgZn-based metallic glass powders. *Sci. Rep.* **2012**, *2*, 418.
(22) Iqbal, M.; Wang, W. H. Synthesis and characterization of Mg-based amorphous alloys and their use for decolorization of Azo dyes. *IOP Conf. Ser.: Mater. Sci. Eng.* **2014**, *60*, 012035.
(23) Zhao, Y. F.; Si, J. J.; Song, J. G.; Yang, Q.; Hui, X. D. Synthesis of Mg-Zn-Ca metallic glasses by gas-atomization and their excellent capability in degrading azo dyes. *Mater. Sci. Eng., B* **2014**, *181*, 46−55.
(24) Ramya, M.; Karthika, M.; Selvakumar, R.; Raj, B.; Ravi, K. R. A facile and efficient single step ball milling process for synthesis of partially amorphous Mg-Zn-Ca alloy powders for dye degradation. *J. Alloys Compd.* **2017**, *696*, 185−192.
(25) Luo, X. K.; Li, R.; Zong, J. Z.; Zhang, Y.; Li, H. F.; Zhang, T. Enhanced degradation of azo dye by nanoporous-copper-decorated Mg-Cu-Y metallic glass powder through dealloying pretreatment. *Appl. Surf. Sci.* **2014**, *305*, 314−320.
(26) Deng, Z.; Zhang, C.; Liu, L. Chemically dealloyed MgCuGd metallic glass with enhanced catalytic activity in degradation of phenol. *Intermetallics* **2014**, *52*, 9−14.
(27) Wang, P. P.; Wang, J. Q.; Li, H.; Yang, H.; Huo, J. T.; Wang, J. G.; Chang, C. T.; Wang, X. M.; Li, R. W.; Wang, G. Fast decolorization of azo dyes in both alkaline and acidic solutions by Al-based metallic glasses. *J. Alloys Compd.* **2017**, *701*, 759−767.
(28) Das, S.; Garrison, S.; Mukherjee, S. Bi-Functional Mechanism in Degradation of Toxic Water Pollutants by Catalytic Amorphous Metals. *Adv. Eng. Mater.* **2016**, *18* (2), 214−218.
(29) Wang, Q. Q.; Chen, M. X.; Lin, P. H.; Cui, Z. Q.; Chu, C. L.; Shen, B. L. Investigation of FePC amorphous alloys with self-renewing behaviour for highly efficient decolorization of methylene blue. *J. Mater. Chem. A* **2018**, *6*, 10686.
(30) Liang, S. X.; Jia, Z.; Liu, Y. J.; Zhang, W. C.; Wang, W. M.; Lu, J.; Zhang, L. C. Compelling Rejuvenated Catalytic Performance in Metallic Glasses. *Adv. Mater.* **2018**, *30* (45), 1802764.
(31) Yoshizawa, Y.; Oguma, S.; Yamauchi, K. New Fe-Based Soft Magnetic-Alloys Composed of Ultrafine Grain-Structure. *J. Appl. Phys.* **1988**, *64* (10), 6044−6046.
(32) Kong, F. L.; Wang, A. D.; Fan, X. D.; Men, H.; Shen, B. L.; Xie, G. Q.; Makino, A.; Inoue, A. High Bs $Fe_{84-x}Si_4B_8P_4Cu_x$(x = 0−1.5) nanocrystalline alloys with excellent magnetic softness. *J. Appl. Phys.* **2011**, *109* (7), 07A303.
(33) Miao, X. F.; Wang, Y. G.; Guo, M. Structural, thermal and magnetic properties of Fe-Si-B-P-Cu melt-spun ribbons: Application of non-isothermal kinetics and the amorphous random anisotropy model. *J. Alloys Compd.* **2011**, *509* (6), 2789−2792.
(34) Dan, Z. H.; Qin, F. X.; Zhang, Y.; Makino, A.; Chang, H.; Hara, N. Mechanism of active dissolution of nanocrystalline Fe-Si-B-P-Cu soft magnetic alloys. *Mater. Charact.* **2016**, *121*, 9−16.
(35) Cao, C. C.; Zhu, L.; Meng, Y.; Zhai, X. B.; Wang, Y. G. Atomic level structural modulation during the structural relaxation and its effect on magnetic properties of Fe81Si4B10P4Cu1 nanocrystalline alloy. *J. Magn. Magn. Mater.* **2018**, *456*, 274−280.
(36) Jia, Z.; Wang, J. C.; Liang, S. X.; Zhang, W. C.; Wang, W. M.; Zhang, L. C. Activation of peroxymonosulfate by $Fe_{78}Si_9B_{13}$ metallic glass: The influence of crystallization. *J. Alloys Compd.* **2017**, *728*, 525−533.
(37) Fu, C. Q.; Xu, L. J.; Dan, Z. H.; Qin, F. X.; Makino, A.; Chang, H.; Hara, N. Annealing effect of amorphous Fe-Si-B-P-Cu precursors on microstructural evolution and redox behavior of nanoporous counterparts. *J. Alloys Compd.* **2017**, *726*, 810−819.
(38) Martinez-Huitle, C. A.; Brillas, E. Decontamination of wastewaters containing synthetic organic dyes by electrochemical methods: A general review. *Appl. Catal., B* **2009**, *87* (3−4), 105−145.
(39) Su, Y. F.; Wu, Z.; Wu, Y. N.; Yu, J. D.; Sun, L.; Lin, C. J. Acid Orange II degradation through a heterogeneous Fenton-like reaction using Fe-TiO_2 nanotube arrays as a photocatalyst. *J. Mater. Chem. A* **2015**, *3* (16), 8537−8544.
(40) Villa, K.; Parmar, J.; Vilela, D.; Sanchez, S. Metal-Oxide-Based Microjets for the Simultaneous Removal of Organic Pollutants and Heavy Metals. *ACS Appl. Mater. Interfaces* **2018**, *10* (24), 20478−20486.
(41) Yavari, A. R.; Le Moulec, A.; Inoue, A.; Nishiyama, N.; Lupu, N.; Matsubara, E.; Botta, W. J.; Vaughan, G.; Di Michiel, M.; Kvick, A. Excess free volume in metallic glasses measured by X-ray diffraction. *Acta Mater.* **2005**, *53* (6), 1611−1619.
(42) Qin, C. L.; Hu, Q. F.; Li, Y. Y.; Wang, Z. F.; Zhao, W. M.; Louzguine-Luzgin, D. V.; Inoue, A. Novel bioactive Fe-based metallic glasses with excellent apatite-forming ability. *Mater. Sci. Eng., C* **2016**, *69*, 513−521.
(43) Rueda, F.; Mendialdua, J.; Rodriguez, A.; Casanova, R.; Barbaux, Y.; Gengembre, L.; Jalowiecki, L. Characterization of Venezuelan laterites by X-ray photoelectron spectroscopy. *J. Electron Spectrosc. Relat. Phenom.* **1996**, *82* (3), 135−143.
(44) Lo, P. H.; Tsai, W. T.; Lee, J. T.; Hung, M. P. The Electrochemical-Behavior of Electroless-Plated Ni-P Alloys in Concentrated Naoh Solution. *J. Electrochem. Soc.* **1995**, *142* (1), 91−96.
(45) Dan, Z. H.; Yamada, Y.; Zhang, Y.; Nishijima, M.; Hara, N.; Matsumoto, H.; Makino, A. Electrochemical Behavior of Annealed Soft-Magnetic Fe-Si-B-P-Cu Alloy. *Mater. Trans.* **2013**, *54* (4), 561−565.
(46) Powell, C. J. Recommended Auger parameters for 42 elemental solids. *J. Electron Spectrosc. Relat. Phenom.* **2012**, *185* (1−2), 1−3.
(47) Hammond, J. S.; Holubka, J. W.; Devries, J. E.; Dickie, R. A. The Application of X-Ray Photoelectron-Spectroscopy to a Study of Interfacial Composition in Corrosion-Induced Paint De-Adhesion. *Corros. Sci.* **1981**, *21* (3), 239−253.
(48) Fujiwara, T. Electronic-Structure in Amorphous Fe, Fe_xP_{1-x} and Fe_xB_{1-x}. *J. Phys. F: Met. Phys.* **1982**, *12* (4), 661−675.
(49) Dan, Z. H.; Takenaka, K.; Zhang, Y.; Unami, S.; Takeuchi, A.; Hara, N.; Makino, A. Effect of Si addition on the corrosion properties of amorphous Fe-based soft magnetic alloys. *J. Non-Cryst. Solids* **2014**, *402*, 36−43.
(50) Atik, M.; De Lima Neto, P.; Aegerter, M. A.; Avaca, L. A. Sol-Gel TiO_2-SiO_2 Films as Protective Coatings against Corrosion of 316l Stainless-Steel in H2so4 Solutions. *J. Appl. Electrochem.* **1995**, *25* (2), 142−148.
(51) Jia, Z.; Kang, J.; Zhang, W. C.; Wang, W. M.; Yang, C.; Sun, H.; Habibi, D.; Zhang, L. C. Surface aging behaviour of Fe-based amorphous alloys as catalysts during heterogeneous photo Fenton-like process for water treatment. *Appl. Catal., B* **2017**, *204*, 537−547.
(52) Kuo, W. G. Decolorizing Dye Waste-Water with Fenton Reagent. *Water Res.* **1992**, *26* (7), 881−886.
(53) Wang, X. F.; Pan, Y.; Zhu, Z. R.; Wu, J. L. Efficient degradation of rhodamine B using Fe-based metallic glass catalyst by Fenton-like process. *Chemosphere* **2014**, *117*, 638−643.
(54) Tang, Y.; Shao, Y.; Chen, N.; Yao, K. F. Rapid decomposition of Direct Blue 6 in neutral solution by Fe-B amorphous alloys. *RSC Adv.* **2015**, *5* (8), 6215−6221.
(55) Chen, J. X.; Zhu, L. Z. Heterogeneous UV-Fenton catalytic degradation of dyestuff in water with hydroxyl-Fe pillared bentonite. *Catal. Today* **2007**, *126* (3−4), 463−470.
(56) Jia, Z.; Zhang, W. C.; Wang, W. M.; Habibi, D.; Zhang, L. C. Amorphous $Fe_{78}Si_9B_{13}$ alloy: An efficient and reusable photo-enhanced Fenton-like catalyst in degradation of cibacron brilliant red 3B-A dye under UV-vis light. *Appl. Catal., B* **2016**, *192*, 46−56.
(57) Jia, Z.; Liang, S. X.; Zhang, W. C.; Wang, W. M.; Yang, C.; Zhang, L. C. Heterogeneous photo Fenton-like degradation of cibacron brilliant red 3B-A dye using amorphous $Fe_{78}Si_9B_{13}$ and

DOI: 10.1021/acsanm.8b01669
ACS Appl. Nano Mater. 2019, 2, 214−227

$Fe_{73.5}Si_{13.5}B_9Cu_1Nb_3$ alloys: The influence of adsorption. *J. Taiwan Inst. Chem. Eng.* **2017**, *71*, 128−136.
(58) Matsuura, M.; Nishijima, M.; Takenaka, K.; Takeuchi, A.; Ofuchi, H.; Makino, A. Evolution of fcc Cu clusters and their structure changes in the soft magnetic $Fe_{85.2}Si_1B_9P_4Cu_{0.8}$ (NANOMET) and FINEMET alloys observed by X-ray absorption fine structure. *J. Appl. Phys.* **2015**, *117* (17), 17A324.
(59) Liang, S. X.; Jia, Z.; Zhang, W. C.; Wang, W. M.; Zhang, L. C. Rapid malachite green degradation using $Fe_{73.5}Si_{13.5}B_9Cu_1Nb_3$ metallic glass for activation of persulfate under UV-Vis light. *Mater. Des.* **2017**, *119*, 244−253.

DOI: 10.1021/acsanm.8b01669
ACS Appl. Nano Mater. 2019, 2, 214−227